HAL
open science

Forced vibrations and wave propagation in multilayered solid spheres using a one-dimensional semi-analytical finite element method

Matthieu Gallezot, Fabien Treyssede, Odile Abraham

▶ **To cite this version:**

Forced vibrations and wave propagation in multilayered solid spheres using a one-dimensional semi-analytical finite element method

Matthieu Gallezot[a,b,*], Fabien Treyssède[b], Odile Abraham[b]

[a]*Université de Nantes, Institut de Recherche en Génie Civil et Mécanique, BP 92208, Nantes, France*
[b]*IFSTTAR, GERS, GeoEND, F-44344, Bouguenais, France*

Abstract

A numerical model is proposed to compute the eigenmodes and the forced response of multilayered elastic spheres. The main idea is to describe analytically the problem along the angular coordinates with spherical harmonics and to discretize the radial direction with one-dimensional finite elements. The proper test function must be carefully chosen so that both vector and tensor spherical harmonics orthogonality relationships can be used. The proposed approach yields a general one-dimensional formulation with a fully analytical description of the angular behaviour, suitable for any interpolating technique. A linear eigenvalue problem, simple and fast to solve, is then obtained. The eigensolutions are the spheroidal and torsional modes. They are favourably compared with literature results for a homogeneous sphere. The eigensolutions are superposed to compute explicitly the forced response. The latter is used to reconstruct the propagation of surfaces waves. In particular, the col-

*Corresponding author
Email address: `matthieu.gallezot@ifsttar.fr` (Matthieu Gallezot)

limation of a Rayleigh wave (non-diffracted surface wave propagating with a quasi-constant width) excited by a line source in a homogeneous sphere is recovered with the model. Based on the vibration eigenmodes, a modal analysis shows that such a wave is a superposition of fundamental spheroidal modes with a displacement confined at the equator of the sphere. These modes are the so-called Rayleigh modes, of sectoral type and high polar wavenumbers. When a thin viscoelastic coating is added to the sphere, the Rayleigh mode behaviour is recovered in a limited frequency range, allowing the generation of a collimating wave at the interface between the sphere and the coating.

1. Introduction

1 The study of the free vibrations (eigenmodes) of an elastic sphere is a
2 classical mechanics problem formally solved first by Lamb [1]. This topic
3 received a great interest in geophysics [2, 3], using the Earth's eigenmodes to
4 synthesize seismograms and improve the understanding of earthquakes [4].
5 Lamb [1] and Shah et al. [5] also studied the case of a hollow sphere (spherical
6 shell), which has been reconsidered with the emergence of composites struc-
7 tures [6–8]. Besides because the eigenmodes are intrinsic to the structure
8 they can be used to characterize unknown materials or geometries, using *e.g.*
9 the resonant scattering theory for immersed spheres [9] or Raman scattering
10 for nanoparticles [10]. Sphere eigenmodes have also found applications in the
11 non-destructive testing of ceramic balls in aeronautics [11].
12 Eigenmodes are the solutions of a dispersion relationship, which can be

obtained analytically in a homogeneous sphere. However advanced numerical methods are required when the structure is complex (*e.g.* multilayered). Buchanan and Ramirez [12] have used a two-dimensional model of the sphere cross-section, using finite elements to discretize the radial and polar angular directions and an exponential ansatz along the azimuthal coordinate. However the computational cost raises quickly with the frequency of interest, and this method is therefore rather limited to low-frequency computation. On the contrary, semi-analytical methods yield a one-dimensional model, and thus the cost remains reasonable even at high frequencies. The basic idea of semi-analytical methods is to describe analytically some directions (in a sphere, the angular ones) and to discretize the remaining one (the radial direction).

This principle has been applied with spherical harmonics along the angular directions and finite elements along the radial direction by Heyliger and Jilani [6] and Park [13]. It leads to a linear eigenvalue problem which is simple to solve. However, both existing formulations do not take full advantage of the analytical description of the solution along the angular coordinates. The eigenproblem of Heyliger and Jilani [6] is not given in a closed-form, so that numerous integrations must be performed before computing the modes. The approach of Park [13] (the so-called spherical thin layer method (STLM)) requires to evaluate, for a given interpolation choice, lengthy analytical expressions of the stiffness matrices. In Park's work, only the conventional linear and quadratic shape functions have been treated. The extension to other interpolating functions is possible, but it would require an important amount of tedious derivations and factorization along the angular coordi-

nates. It is then of interest to propose a more compact formulation in which various interpolating functions can be immediately used, including high-order shape functions (see *e.g.* Ref. [14]).

From the authors' point of view, the main issue is to properly identify the orthogonality relationships of spherical harmonics which must be used to preserve the separation of radial and angular variables in the elastodynamic balance equations. These equilibrium equations correspond to vector wave equations, which complicates the problem. As will be outlined in this paper, two kinds of orthogonality relationships are necessary to eventually obtain a general semi-analytical formulation. On one hand, the orthogonality of vector spherical harmonics is needed for the kinetic energy term (including the scalar product of displacements). This first kind of orthogonality is rather well-known in the literature [15]. On the other hand, the orthogonality of tensor spherical harmonics is required for the potential energy term (including the stress-strain tensor product). This second kind of orthogonality is much more mathematically involved (see *e.g.* Refs. [16, 17]). Note that the principle of semi-analytical methods, when applied to solve the scalar Helmholtz equation (as done in Ref. [18] for instance), is simpler to implement since it only involves the orthogonality of scalar spherical harmonics.

As far as wave propagation is concerned, surface acoustic waves on a sphere are strongly related to the eigenmodes. The latter corresponds to standing waves which naturally occur because of the closed geometry of the sphere. Any wave can be reconstructed by a superposition on the eigen-modes [4, 19]. The Rayleigh surface wave, when excited by a point source, propagates all over the sphere (because of diffraction) and merges at the

pole opposite to the source (because of the curvature). However as shown by Tsukahara et al. [20], Ishikawa et al. [21] and Clorennec and Royer [22], if the source is a line of specific width, the Rayleigh wave is naturally collimated, that is, the wave is not diffracted but propagates with a quasi-constant width. Such a wave makes several roundtrips, which has been exploited to design gas sensors [23]. This phenomenon can be explained as a balance between diffraction and curvature effects. In this paper, we are interested in modelling the propagation of waves excited by an arbitrary source, based on the eigenvibrations of a multilayered sphere. In particular, we want to reproduce the collimation of a Rayleigh wave generated by a line source in a homogeneous sphere, and to investigate the perturbation induced by the addition of a thin viscoelastic coating to the sphere.

The main objective of this paper is to elaborate a general one-dimensional semi-analytical finite element model to compute both the free (eigenmodes) and forced responses of an elastic sphere of complex internal structure (*e.g.* multilayered). This model is presented in Sec. 2 of this paper. The forced response model is calculated explicitly based on modal superposition on the eigenmodes. It is subsequently used to reconstruct the propagation of surface waves. In Sec. 3, the computed eigenmodes are compared with literature results. The forced response is used in Sec. 4 to simulate a collimating Rayleigh wave. The behaviour of this wave is analysed in terms of the eigenvibrations of the sphere. Finally, the effect of a viscoelastic coating on the collimating wave is investigated.

2. The numerical model

2.1. Elastodynamic variational formulation

We consider a solid sphere of radius $r = a$. The problem is described in the spherical coordinate system (r, θ, ϕ) shown in Fig. 1. r is the radial direction; θ is the polar or colatitude angle, with $0 \leq \theta \leq \pi$; ϕ is the azimuthal angle, with $0 \leq \phi \leq 2\pi$. A time-harmonic dependance $e^{-j\omega t}$ is chosen for the displacement field, with $\mathbf{u}(r, \theta, \phi) = [u_r(r, \theta, \phi),\ u_\theta(r, \theta, \phi),\ u_\phi(r, \theta, \phi)]^{\mathrm{T}}$. The superscript T denotes matrix transpose. The elastodynamics variational formulation is (see *e.g.* Bathe [24, Chap. 4]):

$$\int_V \delta\epsilon^{\mathrm{T}} \sigma \mathrm{d}V - \omega^2 \int_V \rho \delta\mathbf{u}^{\mathrm{T}} \mathbf{u} \mathrm{d}V = \int_V \delta\mathbf{u}^{\mathrm{T}} \mathbf{f} \mathrm{d}V + \int_{\partial V} \delta\mathbf{u}^{\mathrm{T}} \mathbf{t} \mathrm{d}\partial V, \qquad (1)$$

with $\mathrm{d}V = r^2 \mathrm{d}r \sin\theta \mathrm{d}\theta \mathrm{d}\phi$. $\mathbf{f}$ is the vector of volumic acoustic forces. $\mathbf{t}$ is the vector of stresses on a spherical isosurface of radius $r = a$, such that $\mathrm{d}\partial V = r^2 \sin\theta \mathrm{d}\theta \mathrm{d}\phi$ (note that a stress boundary condition may also be applied on the inner radius, supposed at $r = b$, in case of a hollow sphere). The stress and strain vectors are respectively given by $\sigma = [\sigma_{rr},\ \sigma_{\theta\theta},\ \sigma_{\phi\phi},\ \sigma_{\theta\phi},\ \sigma_{r\phi},\ \sigma_{r\theta}]^{\mathrm{T}}$ and $\epsilon = [\epsilon_{rr},\ \epsilon_{\theta\theta}, \epsilon_{\phi\phi},\ 2\epsilon_{\theta\phi},\ 2\epsilon_{r\phi},\ 2\epsilon_{r\theta}]^{\mathrm{T}}$. The stress-strain relation is $\sigma = \mathbf{C}\epsilon$. $\mathbf{C}$ is the matrix of material properties. The materials can be elastic or viscoelastic. The model is restricted to the case of transversely isotropic

6

materials, such that:

$$
\mathbf{C} =
\begin{bmatrix}
C_{11} & C_{12} & C_{12} & 0 & 0 & 0 \\
C_{12} & C_{\alpha} & C_{23} & 0 & 0 & 0 \\
C_{12} & C_{23} & C_{\alpha} & 0 & 0 & 0 \\
0 & 0 & 0 & C_{44} & 0 & 0 \\
0 & 0 & 0 & 0 & C_{55} & 0 \\
0 & 0 & 0 & 0 & 0 & C_{55}
\end{bmatrix} ,
\tag{2}
$$

where $C_{\alpha} = 2C_{44} + C_{23}$. This restriction is necessary to allow the separation of angular and radial variables in Sec. 2.2. Besides, material properties can vary arbitrarily along the radius only (*e.g.* a sphere made of several homogeneous layers).

The strain-displacement relation is $\epsilon = \mathbf{L}\mathbf{u}$. The operator $\mathbf{L}$ is given by:

$$
\mathbf{L} = \mathbf{L}_r \frac{\partial}{\partial r} + \mathbf{L}_\theta \frac{1}{r} \frac{\partial}{\partial \theta} + \mathbf{L}_\phi \frac{1}{r \sin \theta} \frac{\partial}{\partial \phi} + \frac{1}{r} \mathbf{L}_1 + \frac{\cot \theta}{r} \mathbf{L}_2 ,
\tag{3}
$$

with:

$$
\mathbf{L}_r =
\begin{bmatrix}
1 & 0 & 0 \\
0 & 0 & 0 \\
0 & 0 & 0 \\
0 & 0 & 0 \\
0 & 0 & 1 \\
0 & 1 & 0
\end{bmatrix},
\mathbf{L}_\theta =
\begin{bmatrix}
0 & 0 & 0 \\
0 & 1 & 0 \\
0 & 0 & 0 \\
0 & 0 & 1 \\
0 & 0 & 0 \\
1 & 0 & 0
\end{bmatrix},
\mathbf{L}_\phi =
\begin{bmatrix}
0 & 0 & 0 \\
0 & 0 & 0 \\
0 & 0 & 1 \\
0 & 1 & 0 \\
1 & 0 & 0 \\
0 & 0 & 0
\end{bmatrix},
\mathbf{L}_1 =
\begin{bmatrix}
0 & 0 & 0 \\
1 & 0 & 0 \\
1 & 0 & 0 \\
0 & 0 & 0 \\
0 & 0 & -1 \\
0 & -1 & 0
\end{bmatrix},
\mathbf{L}_2 =
\begin{bmatrix}
0 & 0 & 0 \\
0 & 0 & 0 \\
0 & 1 & 0 \\
0 & 0 & -1 \\
0 & 0 & 0 \\
0 & 0 & 0
\end{bmatrix} .
\tag{4}
$$

2.2. Vector spherical harmonic expansion

Let us first remind that, applying the Helmholtz decomposition theorem, finding the solutions of the homogeneous elastodynamic equations (strong
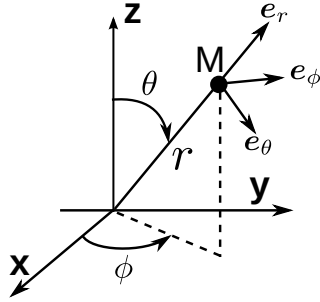
Figure 1: Spherical coordinate system. r: radial coordinate; $0 \leq \theta \leq \pi$: polar or colatitude angle; $0 \leq \phi \leq 2\pi$: azimuthal angle.

formulation) consists in solving three scalar Helmholtz equations. The radial and angular coordinates can be separated, and the angular scalar dependence is written on a basis of spherical harmonic functions [4, 15, 19]. The normalized scalar spherical harmonic functions are given by:

$$Y_l^m(\theta, \phi) = \frac{N_l^m}{\sqrt{2\pi}} P_l^m(\cos\theta) e^{jm\phi} , \tag{5}$$

with the degree l ($l \geq 0$) and the order m ($|m| \leq l$) [25]. $N_l^m = \sqrt{\frac{(2l+1)(l-m)!}{2(l+m)!}}$ is the normalization factor. The integers l and m are also called the polar and azimuthal wavenumbers [4]. $P_l^m(\cos\theta)$ is the associated Legendre polynomial of the first kind, which satisfies the Legendre equation [25]:

$$\frac{d^2 P_l^m}{d\theta^2} + \cot\theta \frac{d P_l^m}{d\theta} + \left(\bar{l} - \frac{m^2}{\sin^2\theta} \right) P_l^m = 0 , \tag{6}$$

with $\bar{l} = l(l+1)$. The explicit form of associated Legendre polynomials is written by convention [25]:

$$P_l^m(\cos\theta) = (-1)^m (\sin\theta)^m \frac{d^m}{d(\cos\theta)^m} P_l(\cos\theta) , \tag{7}$$

where $P_l(\cos\theta)$ is the Legendre polynomial of the first kind, including the Condon-Shortley phase $(-1)^m$.

8

From the scalar solutions, one can eventually obtain the vector displacement solution in which radial and angular variables are also separated. In this paper, the radial behaviour of the displacement is interpolated using finite elements (see Sec. 2.3) instead of using exact spherical Bessel function, while the analytical description of the angular behaviour, using vector spherical harmonics, is exploited.

In Eq. (1), the displacement field is then written as:

$$\mathbf{u}(r,\theta,\phi) = \sum_{l\geq 0} \sum_{|m|\leq l} \mathbf{S}_l^m(\theta,\phi)\hat{\mathbf{u}}_l^m(r)\,, \tag{8}$$

where $\hat{\mathbf{u}}_l^m(r) = [\hat{u}_l^m(r),\ \hat{v}_l^m(r),\ \hat{w}_l^m(r)]^{\mathrm{T}}$ is the vector of the (l,m)–coefficients of the expansion (to be determined). The matrix $\mathbf{S}_l^m$ conveniently concatenates the vector spherical harmonics and is given by [13, 15]:

$$\mathbf{S}_l^m(\theta,\phi) = \begin{bmatrix} \mathrm{Y}_l^m(\theta,\phi) & 0 & 0 \\ 0 & \frac{\partial \mathrm{Y}_l^m(\theta,\phi)}{\partial\theta} & -\frac{\partial \mathrm{Y}_l^m(\theta,\phi)}{\sin\theta\partial\phi} \\ 0 & \frac{\partial \mathrm{Y}_l^m(\theta,\phi)}{\sin\theta\partial\phi} & \frac{\partial \mathrm{Y}_l^m(\theta,\phi)}{\partial\theta} \end{bmatrix}\,. \tag{9}$$

The same form is also assumed for the volumic forces and the normal stresses, that is:

$$\mathbf{f}(r,\theta,\phi) = \sum_{l\geq 0} \sum_{|m|\leq l} \mathbf{S}_l^m(\theta,\phi)\hat{\mathbf{f}}_l^m(r)\,, \tag{10}$$

$$\mathbf{t}(\theta,\phi) = \sum_{l\geq 0} \sum_{|m|\leq l} \mathbf{S}_l^m(\theta,\phi)\hat{\mathbf{t}}_l^m\,. \tag{11}$$

It is noteworthy that the vector spherical harmonics form an orthogonal basis [15, 17], with:

$$\int_0^\pi \int_0^{2\pi} \mathbf{S}_k^{p*}\mathbf{S}_l^m \mathrm{d}\phi \sin\theta \mathrm{d}\theta = \begin{bmatrix} 1 & 0 & 0 \\ 0 & \bar{l} & 0 \\ 0 & 0 & \bar{l} \end{bmatrix} \delta_{kl}\delta_{mp}\,, \tag{12}$$

9

where $*$ stands for the transpose conjugate matrix. The proof is briefly recalled in Appendix A.1. As explained later, the key point of the formulation proposed in this paper is then to choose the test function as follows:

$$\delta\mathbf{u}^{\mathrm{T}}(r,\theta,\phi) = \delta\hat{\mathbf{u}}^{\mathrm{T}}(r)\mathbf{S}_k^{p*}(\theta,\phi)\,. \tag{13}$$

From Eq. (13), one can write the virtual strains as: $\delta\epsilon^{\mathrm{T}} = \left[\mathbf{L}\mathbf{S}_k^{p*\mathrm{T}}\delta\hat{\mathbf{u}}\right]^{\mathrm{T}}$.

2.3. Finite element approximation of the radial dependance of wavefields

Along the radial direction, a finite element approximation is applied such that the displacement on each element is given by:

$$\hat{\mathbf{u}}_l^{m,e}(r) = \mathbf{N}^e(r)\hat{\mathbf{U}}_l^{m,e}\,. \tag{14}$$

$\mathbf{N}^e(r)$ is the matrix of one-dimensional interpolation functions. $\hat{\mathbf{U}}_l^{m,e}$ is the vector of nodal displacements.

In Eq. (1), the angular integrations are then computed and simplified using Eq. (12). To evaluate the integral $\int \delta\epsilon^{\mathrm{T}}\sigma\sin\theta\mathrm{d}\theta\mathrm{d}\phi$, additional relationships coming from the orthogonality of tensor spherical harmonics are necessary. These are given in Appendix A.1. A detailed example is also given in Appendix B for the calculation of one matrix component. Finally, after lengthy algebraic manipulations, the following global matrix system can be obtained:

$$\left(\mathbf{K}(l) - \omega^2\mathbf{M}(l)\right)\hat{\mathbf{U}}_l^m = \hat{\mathbf{F}}_l^m\,. \tag{15}$$

The stiffness matrix is given by:

$$\mathbf{K}(l) = \mathbf{K}_1(l) + \mathbf{K}_2(l) + \mathbf{K}_2^{\mathrm{T}}(l) + \mathbf{K}_3(l)\,, \tag{16}$$

10

where elementary matrices are:

$$\mathbf{K}_1^e(l) = \int \frac{\mathrm{d}\mathbf{N}^{e\mathrm{T}}}{\mathrm{d}r} \begin{bmatrix} C_{11} & 0 & 0 \\ 0 & \bar{l}C_{55} & 0 \\ 0 & 0 & \bar{l}C_{55} \end{bmatrix} \frac{\mathrm{d}\mathbf{N}^e}{\mathrm{d}r} r^2 \mathrm{d}r\,, \tag{17}$$

$$\mathbf{K}_2^e(l) = \int \frac{\mathrm{d}\mathbf{N}^{e\mathrm{T}}}{\mathrm{d}r} \begin{bmatrix} 2C_{12} & -\bar{l}C_{12} & 0 \\ \bar{l}C_{55} & -\bar{l}C_{55} & 0 \\ 0 & 0 & -\bar{l}C_{55} \end{bmatrix} \mathbf{N}^e r \mathrm{d}r\,, \tag{18}$$

$$\mathbf{K}_3^e(l) = \int \mathbf{N}^{e\mathrm{T}} \begin{bmatrix} \bar{l}C_{55} + 4C_\beta & -\bar{l}\big(C_{55} + 2C_\beta\big) & 0 \\ -\bar{l}\big(C_{55} + 2C_\beta\big) & \bar{l}(C_{55} + \bar{l}C_{23} + 2(\bar{l}-1)C_{44}) & 0 \\ 0 & \bar{l}(C_{55} + (\bar{l}-2)C_{44}) & 0 \end{bmatrix} \mathbf{N}^e \mathrm{d}r\,, \tag{19}$$

where $C_\beta = C_{23} + C_{44}$.

The elementary mass matrix is given by:

$$\mathbf{M}^e(l) = \int \rho \mathbf{N}^{e\mathrm{T}} \begin{bmatrix} 1 & 0 & 0 \\ 0 & \bar{l} & 0 \\ 0 & 0 & \bar{l} \end{bmatrix} \mathbf{N}^e r^2 \mathrm{d}r\,. \tag{20}$$

The force vector $\hat{\mathbf{F}}_l^m$ gathers the contribution of volumic forces and stresses, that is:

$$\hat{\mathbf{F}}_l^m = \hat{\mathbf{F}}_{l,v}^m + \hat{\mathbf{F}}_{l,s}^m\,. \tag{21}$$

The elementary volumic forces are given by:

$$\hat{\mathbf{F}}_{l,v}^{m,e} = \int \mathbf{N}^{e\mathrm{T}} \begin{bmatrix} 1 & 0 & 0 \\ 0 & \bar{l} & 0 \\ 0 & 0 & \bar{l} \end{bmatrix} \hat{\mathbf{f}}_l^{m,e} r^2 \mathrm{d}r\,. \tag{22}$$

11

The contribution of stresses can be written:

$$\delta\hat{\mathbf{U}}^{\mathrm{T}}\hat{\mathbf{F}}_{l,s}^{m} = \begin{bmatrix} 1 & 0 & 0 \\ 0 & \bar{l} & 0 \\ 0 & 0 & \bar{l} \end{bmatrix} \left[\delta\hat{\mathbf{u}}r^2\hat{\mathbf{t}}_l^m\right]_{r=b}^{r=a} , \tag{23}$$

where $\delta\hat{\mathbf{U}}$ is the vector of virtual nodal displacements.

As a final remark, let us highlight the significance of the test function (13). Owing to this choice, the orthogonality of vector spherical harmonics (Eq. (12)) immediately appears in each integral of Eq. (1). Moreover, this choice also takes advantage of the orthogonality of tensor spherical harmonics [16, 17], which leads to the identities summed up by Eqs. (A.4)–(A.5) in Appendix A.1. Both vector and tensor orthogonality relationships are mandatory to get uncoupled governing equations for each pair of wavenumbers (l, m), as eventually obtained in Eq. (15). This yields a general formulation with a fully analytical description of the problem along the two angular coordinates. This is not the case in the model of Heyliger and Jilani [6], in which angular integrals must be solved analytically or numerically for each value of l. On the other hand, compared with the formulation of Park [13], the expressions of the matrices given by Eqs. (17)–(19) are valid for any choice of interpolation functions.

2.4. The source-free problem: computation of the eigenmodes

To compute the eigenmodes of the sphere, the source-free problem must be considered (*i.e.* $\hat{\mathbf{F}}_l^m = \mathbf{0}$ in Eq. (15)). It yields a standard linear eigenproblem in terms of ω. For each integer value of l, one obtains N eigenfrequencies $\omega_l^{(n)}$ and eigenvectors $\hat{\mathbf{U}}_l^{(n)}$ (corresponding to the radial mode shapes), with $n = 1 \ldots N$.

12

Let us stress than when this problem is solved analytically, the eigenfrequencies are the roots of transcendental equations involving spherical Bessel functions (the dispersion relationship can be found for a homogeneous and isotropic sphere in Ref. [19]), which must be solved with root-finding algorithms. Their convergence can be poor at high frequencies because of instabilities [26]. Conversely, the linear eigenproblem obtained in this paper can be solved with standard methods.

The eigenproblem shares some properties with the analytical dispersion relationship. Both are degenerate with respect to the azimuthal wavenumber m, such that there are $2l+1$ independent modes with the same eigenfrequency $\omega_l^{(n)}$ [27, 28]. Furthermore, it can be noticed from the structures of matrices in Eqs. (17)–(20) that the eigensystem can be readily divided into two independent linear eigenproblems, namely:

$$(\mathbf{K}_S - \omega^2 \mathbf{M}_S)\hat{\mathbf{U}}_S = \mathbf{0} \,, \tag{24}$$

$$(\mathbf{K}_T - \omega^2 \mathbf{M}_T)\hat{\mathbf{U}}_T = \mathbf{0} \,. \tag{25}$$

One recovers the two families of eigenmodes in a sphere [19]. The first eigenproblem yields the so-called spheroidal modes, which have a non-zero displacement in every direction. The second eigenproblem yields the so-called torsional modes, which have a non-zero displacement only in the angular (transverse) directions. For the simplicity of the formulation, this decomposition is not exploited in this paper (the finite element discretization is only one-dimensional and leads to fast computations).

2.5. The forced response: wave propagation

To reconstruct surface wave propagation, the forced response problem

must be considered. First, let us write the linear eigenproblem for a given

mode (l, n):

$$(\mathbf{K}(l) - \omega_l^{(n)2}\mathbf{M}(l))\hat{\mathbf{U}}_l^{(n)} = \mathbf{0} \,. \tag{26}$$

Owing to viscoelasticity (if any), the matrices $\mathbf{K}$ and $\mathbf{M}$ are complex-valued

and not Hermitian. However, both matrices are symmetric such that the

following orthogonality relationships hold:

$$\hat{\mathbf{U}}_l^{(k)\mathrm{T}}\mathbf{K}(l)\hat{\mathbf{U}}_l^{(n)} = \omega_l^{(n)2}\delta_{kn} \,, \tag{27}$$

$$\hat{\mathbf{U}}_l^{(k)\mathrm{T}}\mathbf{M}(l)\hat{\mathbf{U}}_l^{(n)} = \delta_{kn} \,. \tag{28}$$

Introducing the modal expansion $\hat{\mathbf{U}}_l^m = \sum_{n=1}^{N} \alpha^{(n)}\hat{\mathbf{U}}_l^{(n)}$ into the forced re-

sponse equation (15), multiplying by $\hat{\mathbf{U}}_l^{(k)\mathrm{T}}$ and using the orthogonality re-

lationships (27) and (28) yields:

$$\alpha^{(n)} = \frac{\hat{\mathbf{U}}_l^{(n)\mathrm{T}}\hat{\mathbf{F}}_l^m}{\omega_l^{(n)2} - \omega^2} \,, \tag{29}$$

such that:

$$\hat{\mathbf{U}}_l^m = \sum_{n=1}^{N} \frac{\hat{\mathbf{U}}_l^{(n)\mathrm{T}}\hat{\mathbf{F}}_l^m\hat{\mathbf{U}}_l^{(n)}}{\omega_l^{(n)2} - \omega^2} \,. \tag{30}$$

This quantity corresponds at each node to the displacement Frequency Re-

sponse Function (FRF) of a pair (l, m). Its inverse Fourier transform yields

the transient displacement:

$$\hat{\mathbf{U}}_l^m(t) = \frac{1}{2\pi}\int_{-\infty}^{+\infty}\left[\sum_{n=1}^{N}\frac{\hat{\mathbf{U}}_l^{(n)\mathrm{T}}\hat{\mathbf{F}}_l^m(\omega)\hat{\mathbf{U}}_l^{(n)}}{\omega_l^{(n)2} - \omega^2}\right]\mathrm{e}^{-\mathrm{j}\omega t}\mathrm{d}\omega \,. \tag{31}$$

Finally, the vector of physical nodal displacements in the time domain is given by:

$$\mathbf{U}(\theta, \phi, t) = \sum_{l \geq 0} \sum_{|m| \leq l} \mathbf{S}_l^m(\theta, \phi) \hat{\mathbf{U}}_l^m(t) \,. \tag{32}$$

2.6. Wave properties

Phase and group velocities can be derived from the eigenfrequencies. The phase velocity is given by:

$$v_{p_l}^{(n)} = \frac{\mathrm{Re}(\omega_l^{(n)}) a}{l + \frac{1}{2}} \,, \tag{33}$$

where $ka = l + 1/2$ accounts for the polar phase-shift of surface waves [19, 29].

The group velocity is defined as [19]:

$$v_{g_l}^{(n)} = \mathrm{Re} \frac{\partial \omega_l^{(n)}}{\partial l} a \,, \tag{34}$$

Following Finnveden [30], the group velocity can be obtained from the finite element matrices (which avoids complex mode sorting). Deriving Eq. (26) with respect to l yields:

$$\left(\frac{\partial \mathbf{K}(l)}{\partial l} - 2\omega_l^{(n)} \mathbf{M}(l) \frac{\partial \omega_l^{(n)}}{\partial l} - \omega_l^{(n)2} \frac{\partial \mathbf{M}(l)}{\partial l} \right) \hat{\mathbf{U}}_l^{(n)}$$
$$+ (\mathbf{K}(l) - \omega_l^{(n)2} \mathbf{M}(l)) \frac{\partial \hat{\mathbf{U}}_l^{(n)}}{\partial l} = 0 \,. \tag{35}$$

Multiplying by $\hat{\mathbf{U}}_l^{(n)\mathrm{T}}$, the second term is equal to zero. One readily obtains the following expression:

$$v_{g_l}^{(n)} = \mathrm{Re} \left[\frac{\hat{\mathbf{U}}_l^{(n)\mathrm{T}} \left(\frac{\partial \mathbf{K}(l)}{\partial l} - \omega_l^{(n)2} \frac{\partial \mathbf{M}(l)}{\partial l} \right) \hat{\mathbf{U}}_l^{(n)}}{2\omega_l^{(n)} \hat{\mathbf{U}}_l^{(n)\mathrm{T}} \mathbf{M}(l) \hat{\mathbf{U}}_l^{(n)}} \right] a \,. \tag{36}$$

15

To compute the derivative of the mass and the stiffness matrices, it is noteworthy that they can be readily factored as:

$$\mathbf{K}(l) = \mathbf{K}_1' + \bar{l}(\mathbf{K}_2' + \mathbf{K}_2'^{\mathrm{T}}) + \bar{l}^2 \mathbf{K}_3' \,, \tag{37}$$

$$\mathbf{M}(l) = \mathbf{M}_1' + \bar{l}\mathbf{M}_2' \,. \tag{38}$$

Therefore, their derivatives are given by:

$$\frac{\partial \mathbf{K}(l)}{\partial l} = (2l+1)(\mathbf{K}_2' + \mathbf{K}_2'^{\mathrm{T}}) + 2\bar{l}(2l+1)\mathbf{K}_3' \,, \tag{39}$$

$$\frac{\partial \mathbf{M}(l)}{\partial l} = (2l+1)\mathbf{M}_2' \,. \tag{40}$$

2.7. Remarks on the sherical harmonic expansion

In Eqs. (8), (10), (11), the quantities $\hat{\mathbf{u}}_l^m$, $\hat{\mathbf{f}}_l^m$, $\hat{\mathbf{t}}_l^m$ stand for the coefficients of a Vector Spherical Harmonic Transform (Vector SHT analysis), given by:

$$\hat{\mathbf{u}}_l^m(r) = \int_0^\pi \int_0^{2\pi} \mathbf{S}_l^{m*}(\theta, \phi)\mathbf{u}(r, \theta, \phi)\mathrm{d}\phi \sin\theta \mathrm{d}\theta \,. \tag{41}$$

Accordingly the physical quantities $\mathbf{u}_l^m$, $\mathbf{f}_l^m$, $\mathbf{t}_l^m$ are the results of an Inverse Vector Spherical Harmonic Transform (Vector SHT synthesis). As shown by Kostelec et al. [31], the θ-derivative of Y_l^m in $\mathbf{S}_l^m$ can be related recursively to the $l+1$ and $l-1$ spherical harmonics degrees, such that the vector SHT is equivalent to several scalar SHT. For any scalar function $h(\theta, \phi)$, its SHT synthesis is:

$$h(\theta, \phi) = \sum_{l \geq 0} \sum_{|m| \leq l} Y_l^m(\theta, \phi)\hat{h}_l^m \,. \tag{42}$$

The complex-valued coefficients $\hat{h}_l^m$ can be obtained from the SHT analysis of the function h, that is:

$$\hat{h}_l^m = \int_0^\pi \int_0^{2\pi} Y_l^{m*}(\theta, \phi)h(\theta, \phi)\mathrm{d}\phi \sin\theta \mathrm{d}\theta \,. \tag{43}$$

16

These transforms cannot be evaluated analytically in general. Several accurate and quick numerical tools have been proposed in the literature [32–34]. In this paper, the SHT analysis and synthesis are performed following the numerical strategy described in Refs. [33] and [34]. The fundamental steps are briefly recalled in the following for self-consistency.

First, Eq. (43) can be written as:

$$\hat{h}_l^m = \frac{N_l^m}{\sqrt{2\pi}} \int_0^\pi \left[\int_0^{2\pi} e^{-\mathrm{j}m\phi} f(\theta, \phi) \mathrm{d}\phi \right] P_l^m(\cos\theta) \sin\theta \mathrm{d}\theta \,. \qquad (44)$$

Equation (44) shows that the SHT analysis can be subdivided into a Fourier transform followed by a projection on the basis of associated Legendre polynomials of the first kind.

The Fourier transform integral is computed using a Discrete Fourier Transform (DFT) on a minimum of $N_{TF} = 2L + 1$ samples along the azimuthal coordinate according to Shannon's theorem, where L is the maximum value of l. In practice, the DFT can be efficiently computed using Fast Fourier Transform (FFT) algorithms [35]. It yields the spectrum of coefficients $h^m(\theta)$.

The projection on the basis of associated Legendre polynomial is then evaluated using a Gauss-Legendre quadrature (GLQ). For a given m and using the change of variable $x = \cos\theta$, one obtains:

$$\int_0^\pi h^m(\theta) P_l^m(\cos\theta) \sin\theta \mathrm{d}\theta = \sum_{q=1}^{L+1} w_q h^m(\mathrm{acos}\, x_q) P_l^m(x_q) \,, \qquad (45)$$

where w_q are the Gauss weights and x_q are the Gauss points. Using $L + 1$ Gauss points, the integration is exact if the product $h^m(\mathrm{acos}\, x_q) P_l^m(x_q)$ is a polynomial of maximum degree $2L$. The latter assumption is not strictly satisfied, but the accuracy has been shown to be very good in practice [33].

17

264 The SHT synthesis (42) can be written as:

$$h(\theta, \phi) = \frac{N_l^m}{\sqrt{2\pi}} \sum_{m=-L}^{m=L} \left[\sum_{l=|m|}^{L} \hat{h}_l^m P_l^m(\cos\theta) \right] e^{jm\phi} . \tag{46}$$

265 This equation shows that for each value of θ the first step of the SHT synthesis
266 is a summation over the associated Legendre polynomial basis, followed by
267 an Inverse DFT. Note that the number of synthesis along θ can be reduced
268 taking advantage of the symmetry of the associated Legendre polynomial
269 across the equator, with the identity:

$$P_l^m(\cos(\pi - \theta)) = (-1)^{(l+m)} P_l^m(\cos\theta) . \tag{47}$$

270 **3. Validation test case: free vibrations of an isotropic homogeneous**
271 **sphere**

Material	E (GPa)	ρ (kg m^{-3})	c_l (m s^{-1})	c_s (m s^{-1})	η_l (Np wavelength^{-1})	η_s (Np wavelength^{-1})
Steel	200	7932	5500.7	3175.8	0.003	0.008
Epoxy	9	1600	2960	1450	0.0047	0.0069

Table 1: Material properties

272 *3.1. Description of the test case*

273 Let us consider an isotropic sphere of radius $a = 10$ mm. The surface of
274 the sphere is free (*i.e.* $\sigma_{rr} = \sigma_{r\theta} = \sigma_{r\phi} = 0$). The sphere is made of steel.
275 Materials properties are given in Table 1 (here the viscoelastic parameters
276 are equal to zero). The material is isotropic and its stiffness matrix can be

18

written as:

$$
\mathbf{C} = \begin{bmatrix} 3\lambda & \lambda & \lambda & 0 & 0 & 0 \\ \lambda & 3\lambda & \lambda & 0 & 0 & 0 \\ \lambda & \lambda & 3\lambda & 0 & 0 & 0 \\ 0 & 0 & 0 & \lambda & 0 & 0 \\ 0 & 0 & 0 & 0 & \lambda & 0 \\ 0 & 0 & 0 & 0 & 0 & \lambda \end{bmatrix},
\tag{48}
$$

with the Lamé's parameter $\lambda = E\nu/[(1+\nu)(1-2\nu)]$ ($\nu = 0.25$).

The eigenmodes computed with the numerical method of this paper are compared with the results of Ref. [19, Ch. 8] for $n = 1, \ldots, 5$ and $l = 1, \ldots, 60$. The non-dimensional eigenfrequencies are defined by $\overline{\omega}_l^{(n)} = a\omega_l^{(n)}/c_S$, where c_S is the shear wave velocity. The radius is discretized with three-nodes line elements of length $\Delta r = 0.012a$, which corresponds to a sixth of the minimum radial wavelength given by $2\pi c_S/\max(\omega_l^{(n)})$. The one-dimensional numerical model then comprises 1014 degrees of freedom (dofs).

3.2. Results

Figure 2 compares the eigenfrequencies of Ref. [19] and those obtained with the numerical method of this paper. Both results are superimposed. The curves of the spheroidal modes (blue triangles in Fig. 2) start at $l = 0$ at breathing mode eigenfrequencies (modes with a radial polarization only). At low wavenumber l, these curves also exhibit a sudden change of slope, characterizing a strong dispersive behaviour.

Some radial modeshapes $\mathbf{U}_l^m$ are displayed in Fig. 3. The dofs $\hat{u}_l^m$, $\hat{v}_l^m$ and $\hat{w}_l^m$ can be related to physical displacements, based on the two independent eigensystems (24)–(25). The dofs $\hat{u}_l^m$ describe the radial dependence of u_r.

19

As expected, they are null for torsional modes which are polarized along the angular directions only – see Fig. 3e. The dofs $\hat{v}_l^m$ give the radial dependence of u_θ and u_ϕ for spheroidal modes. As shown in Fig. 3b,c,d, the dofs $\hat{w}_l^m$ are null in that case. On the contrary, the dofs $\hat{w}_l^m$ are the only non-zero dofs for torsional modes – see Fig. 3e. To verify the accuracy on modeshapes, Fig. 3b can be compared with the results of Ref. [19]. A very good visual agreement is obtained.

The radial behaviour of the modes depends on their polar wavenumber l and on their order n. For $l = 0$, the motion is purely radial (breathing mode) and distributed over the radius (Fig. 3a). The spheroidal modes with $l = 1$ are the only modes with a non-zero displacement at $r = 0$ – see Fig. 3b and [19]. As shown in Fig. 3c and 3d, for high values of l the displacement is confined near the surface, particularly for the fundamental mode with $n = 1$ (Fig. 3c). When the order n of the mode increases, *e.g.* in Fig. 3d with $n = 5$, the inner displacement increases and oscillations can be observed along the radius.

A simple post-processing step enables to represent the modal displacement on a spherical surface (some properties necessary to compute the values of $\mathbf{S}_l^m(\theta, \phi)$ are given in Appendix A.2). Figure 4 shows the normal displacement u_r at the surface of the sphere ($r = a$), for the fundamental spheroidal mode ($n = 1$) with $l = 30$. The displacement is shown for three values of m ($m = 0$, $m = 10$, $m = l = 30$). All the modes have the same eigenfrequency because of the eigensystem degeneracy, but the modeshapes in the angular directions are quite different. These modeshapes correspond to the zonal (Fig. 4a), tesseral (Fig. 4b) and sectoral (Fig. 4c) patterns of the spherical
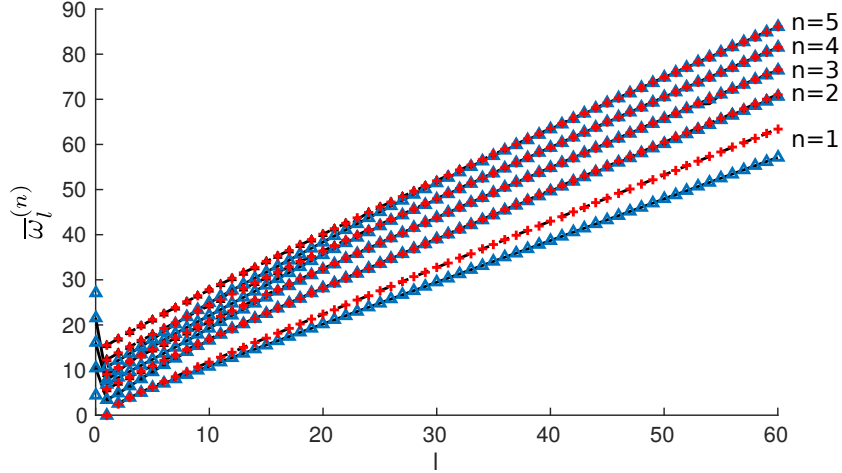
20

Figure 2: Non-dimensional eigenfrequencies $\overline{\omega}_l^{(n)}$ of a surface-free sphere made of steel. Solid and dashed blacked lines: results of Eringen and Şuhubi [19] for spheroidal and torsional modes. Blue triangles: numerical results for spheroidal modes. Red crosses: numerical results for torsional modes.

harmonics [15, 25], modulated by the radial behaviour of the mode. For the angular components u_θ and u_ϕ (not shown here), similar patterns can be observed (some of them then involve the θ-derivative of the patterns of spherical harmonics). It is noteworthy that for high values of l (*i.e.* with a displacement confined at the surface), the sectoral modes appear to be analogue to the so-called whispering-gallery modes, which have found many applications in optics [36–38].

4. Surface Acoustic Waves

In this section, the numerical model is used to reconstruct the collimation of the Rayleigh surface wave, and to interpret this phenomenon in terms of the eigenvibrations of the sphere. As an example of a multilayered sphere,
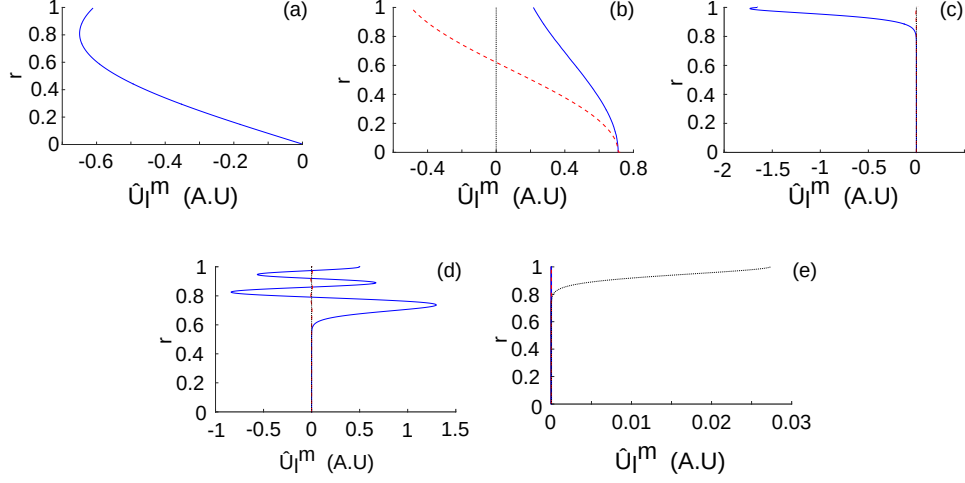
Figure 3: Radial modeshapes (arbitrary unit) $\hat{u}_l^m(r)$ (solid blue line), $\hat{v}_l^m(r)$ (dashed red line) and $\hat{w}_l^m(r)$ (dotted black line) of (a) spheroidal mode, $l = 0$, $n = 1$ ($\overline{\omega}_0^{(1)} = 4.44$); (b) spheroidal mode, $l = 1$, $n = 2$ ($\overline{\omega}_1^{(2)} = 3.412$); (c) spheroidal mode, $l = 60$, $n = 1$ ($\overline{\omega}_{60}^{(1)} = 57.13$); (d) spheroidal mode, $l = 60$, $n = 5$ ($\overline{\omega}_{60}^{(5)} = 86.03$); (e) torsional mode, $l = 60$, $n = 1$ ($\overline{\omega}_{60}^{(1)} = 63.44$).
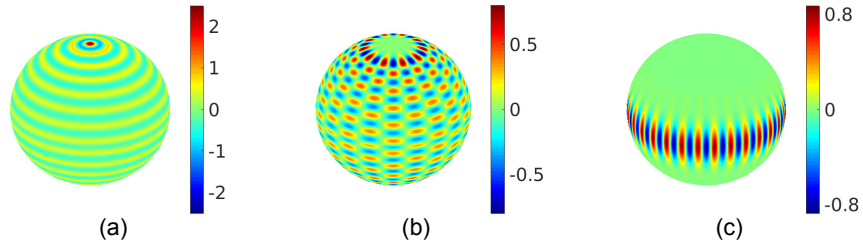
Figure 4: Normal modal displacement (arbitrary unit) $u_r(r = a, \theta, \phi)$ of the fundamental spheroidal modes $l = 30$, $n = 1$ ($\overline{\omega}_{30}^{(1)} = 29.46$) (a) for $m = 0$; (b) for $m = 10$; (c) for $m = l$.

22

³³² the effect of a viscoelastic coating is finally investigated.

4.1. Description of the collimating wave test case

³³⁴ In this test case, an isotropic and homogeneous sphere made of viscoelastic
³³⁵ steel is considered. The material properties are given in Table 1. The radius
³³⁶ of the sphere is $a = 25$ mm. A normal force $F(\theta, \phi, t)\mathbf{e}_r$ is applied at the
³³⁷ surface of the sphere, with:

$$F(\theta, \phi, t) = f(\theta, \phi)g(t). \tag{49}$$

³³⁸ Only spheroidal modes are excited, because the excitation is limited to the
³³⁹ radial direction.

³⁴⁰ The transient part of the force $g(t)$ is a sinus of centre frequency $f_c =$
³⁴¹ 1 MHz modulated over $n = 5$ cycles by a Hanning window. It is given
³⁴² explicitly by:

$$g(t) = \begin{cases} \dfrac{1}{2}\sin(2\pi f_c t)\left[1 + \cos\left(\dfrac{2\pi f_c}{n}t - \pi\right)\right] & \text{if } 0 \leq t \leq \dfrac{n}{f_c}, \\ 0 \text{ if } t > \dfrac{n}{f_c}. \end{cases} \tag{50}$$

³⁴³ $f(\theta, \phi)$ is distributed along a thick line. The line source is modelled by the
³⁴⁴ product of two Gaussian functions as:

$$f(\theta, \phi) = \mathrm{e}^{-\frac{(\theta-\theta_c)^2}{2\theta_\sigma^2}} \, \mathrm{e}^{-\frac{(\phi-\phi_c)^2}{2\phi_\sigma^2}}. \tag{51}$$

³⁴⁵ It is centered at the equator (*i.e.* at $\theta_c = \pi/2$) and at $\phi_c = 0$. The standard
³⁴⁶ deviations θ_σ and ϕ_σ control the width of the Gaussian along the polar and
³⁴⁷ the azimuthal coordinates respectively. One sets $\phi_\sigma = 2\pi/235$ ($\approx 1.5°$) to
³⁴⁸ obtain a thick line perpendicular to the equator.

349 According to Clorennec and Royer [22], it is possible to choose the polar

350 aperture of the source (51) to obtain a collimating Rayleigh wave. In that

351 case, the propagation of the wave is diffraction-free. The Rayleigh wave

352 propagates with a quasi-constant polar width in the direction perpendicular

353 to the source. The collimation angle of the source is given in Ref. [22] by

354 the formula:

$$\theta_{\text{COL}} = \sqrt{\frac{\pi c_R}{4 a f_c}}, \tag{52}$$

355 where $c_R \approx 0.9194 c_S$ is the Rayleigh wave velocity [19]. Here, $c_R \approx 2919.8 \text{ m s}^{-1}$.

356 It yields $\theta_{\text{COL}} \approx 0.3029$ ($\approx 17.3°$). Taking the Gaussian width as $1/e^2$, one

357 sets $\theta_\sigma = 0.1514$ in Eq. (51). For comparison, two other cases are also

358 considered: a longer line source ($\theta_\sigma = 0.2668$) and a shorter line source

359 ($\theta_\sigma = 0.0667$). The waves emitted by these three different sources are com-

360 puted from the modal expansion given in Sec. 2.5.

361 The source term (see Eq. (21)) is obtained from the coefficients $\hat{\mathbf{t}}_l^m$.

362 The latter are computed with a numerical SHT analysis (see Eqs.(44)–(45))

363 applied to Eq. (51) with l from 0 to 150. The GLQ is computed with $L = 151$

364 Gauss points and weights (determined with the function *legpts* of the Chebfun

365 package [39]). The number of FFT points along the azimuthal wavenumber

366 is set to 512. It has been checked that the L2-error over the whole spherical

367 surface between the initial source (given by Eq. (51)) and the synthetized

368 one (inverse SHT of $\hat{\mathbf{t}}_l^m$, applying Eq. (46)) is less than 1%.

369 The length of the one-dimensional finite elements is $\Delta r = 0.003a$, which

370 yields 2 010 dofs. The forced response is obtained with a superposition of

371 $N = 80$ eigenfrequencies. The solution is computed between 0 and 10 MHz
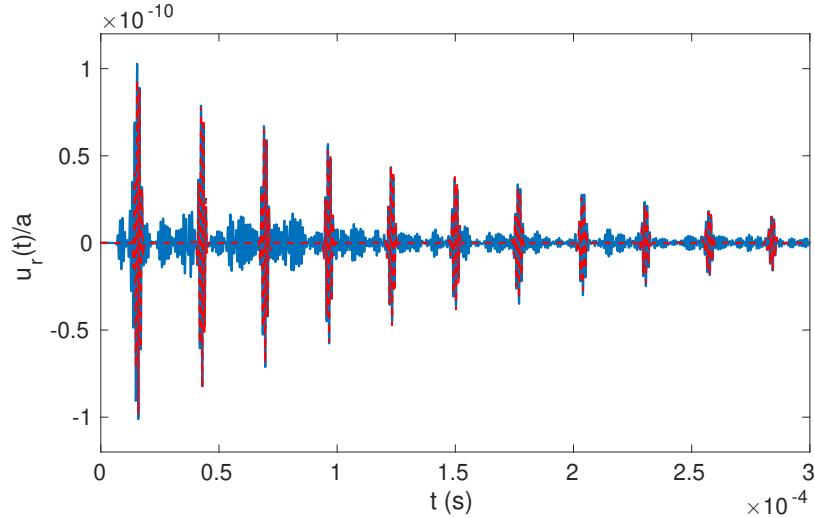
372 for 8 192 frequencies.

24

Figure 5: Transient collimating signal $u_r(t)/a$ at the surface of a viscoelastic sphere ($r = a$) at point $\theta = \pi/2$, $\phi = \pi/2$. Blue curve: modal superposition using $N = 80$ modes. Red dashed curve: modal superposition using the fundamental Rayleigh mode only ($N = 1$). Line source: $\theta_\sigma = 0.1514$.

4.2. Results

4.2.1. Collimating, diverging and focusing waves

Figure 5 shows the transient displacement at the point $\theta = \pi/2$ (on the equator) and $\phi = \pi/2$, for the source with $\theta_\sigma = 0.1514$. Several major peaks can be observed. These peaks correspond to the arrivals of the Rayleigh wave, either propagating counter-clockwise (*e.g.* the first and the third peaks), either propagating clockwise (*e.g.* the second and the fourth peaks). On this figure, the time-of-flight between the peaks is estimated to 27.01 µs, which agrees well with the theoretical arrival of the Rayleigh wave to do a half-trip (26.89 µs).

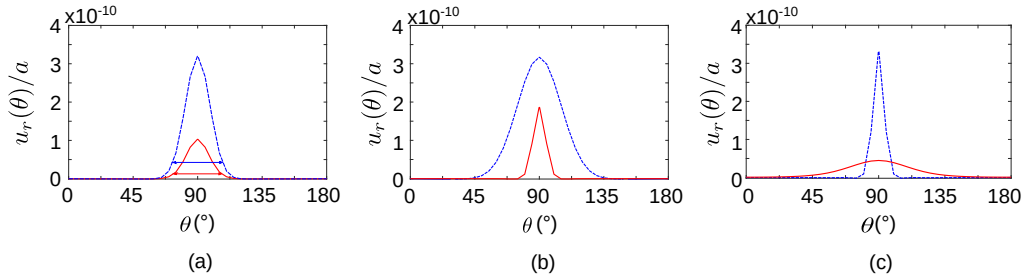Figure 6 represents the normal displacement u_r at the surface as a func-

25

Figure 6: Normal displacement $u_r(\theta)/a$ at the surface of a viscoelastic sphere ($r = a$). Blue dashed curve: at $\phi = 0$ and $t = 2.289$ µs. Red solid curve: at $\phi = \pi/2$ and $t = 15.38$ µs. (a) Collimating wave ($\theta_\sigma = 0.1514$); (b) Focusing wave ($\theta_\sigma = 0.2668$); (c) Diverging wave ($\theta_\sigma = 0.0667$).

tion of the polar angle θ, at $\phi = 0$ (at the source position) and at $\phi = \pi/2$ (after a trip of a quarter of circumference), for the three different sources. In each case, the amplitude is lower at $\phi = \pi/2$ (red curve) than at the source position (blue dashed curve) because of viscoelastic losses (and because the source splits into waves travelling in opposite directions).

For a source width $\theta_\sigma = 0.1514$, the variation of the wavefront width is weak and equal to 6% (see Fig. 6a). A collimating wave is then obtained, as predicted by Eq. (52).

Conversely, the wavefront width strongly decreases when the source is larger ($\theta_\sigma = 0.2668$) – see Fig. 6b. As shown in Fig. 6c, when the source is shorter ($\theta_\sigma = 0.0667$) the wavefront width increases. The propagation is not diffraction-free in these cases. Note that the diffraction reaches its maximum at $\phi = \pi/2$ because it is located right in between the source and its opposite pole. The wave in Fig. 6b is called focusing wave because the wavefront focuses towards $\phi = \pi/2$ and then diverges towards the pole opposite to the source [21]. The so-called diverging wave (Fig. 6c) diverges towards $\phi = \pi/2$
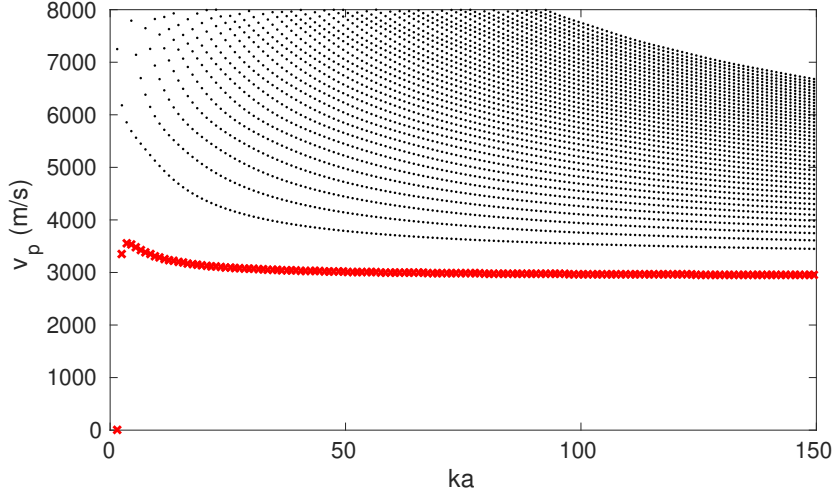
26

Figure 7: Phase velocity of spheroidal modes for a viscoelastic steel sphere of radius $a = 25$ mm. Red crosses: Rayleigh fundamental mode ($n = 1$).

and then converges towards the pole opposite to the source.

Some videos of the transient collimating, diverging and focusing Rayleigh waves are included in the supplementary materials of the electronic version of this paper to clearly visualize these phenomena.

4.2.2. Modal analysis

As described in Sec. 3.2, the displacement of the fundamental spheroidal mode ($n = 1$) is generally confined near the surface. This mode is usually called the Rayleigh mode [22], because its velocity approaches asymptotically the Rayleigh wave velocity in a half-space (see Fig. 7). Retaining only the Rayleigh mode to compute the forced response yields the red curve in Fig. 5, which correctly approximates the main wave packets. Higher-order modes ($n > 1$) enrich the signal with the contribution of other waves which can be identified as body waves travelling inside the sphere [19].
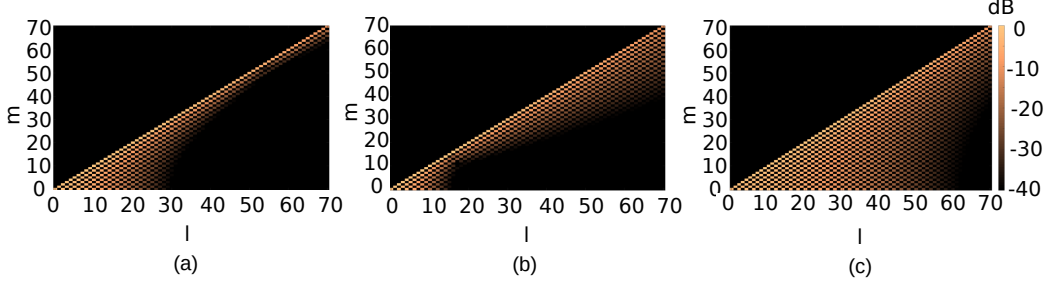
27

Figure 8: Coefficients $10 \log_{10}(|\hat{\mathbf{t}}_l^m / \max \hat{\mathbf{t}}_l^m|)$ (dB) of the force applied to obtain (a) a collimating wave ($\theta_\sigma = 0.1514$); (b) a focusing wave ($\theta_\sigma = 0.2668$); (c) a diverging wave ($\theta_\sigma = 0.0667$). These coefficients are computed from the numerical SHT analysis based on Eq. (45) with l from 0 to 150, 151 GLQ and 512 FFT points.
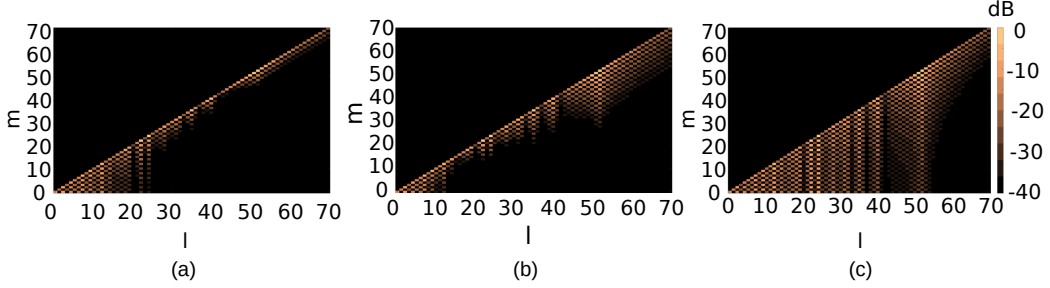

Figure 9: Forced response $10 \log_{10}(|\hat{u}_l^m / \max \hat{u}_l^m|)$ (dB) at the surface of a viscoelastic sphere ($r = a$) and at the centre frequency ($\overline{\omega} = 49.46$) for (a) a collimating wave ($\theta_\sigma = 0.1514$); (b) a focusing wave ($\theta_\sigma = 0.2668$); (c) a diverging wave ($\theta_\sigma = 0.0667$).

Interestingly the modal contributions can be further decomposed as a function of polar and azimuthal wavenumbers l and m. Figure 8 displays the coefficients $|\hat{\mathbf{t}}_l^m|$ of the three different sources. The resulting modal responses $|\hat{u}_l^m(r = a)|$ (see Eq. (30)) at centre frequency $\overline{\omega} = 49.46$ are shown in Fig. 9.

In the collimating case, Fig. 8a and Fig. 9a show that the source mostly excites sectoral modes (*i.e.* with $m \approx l$), except for low values of l ($l < 20$) where tesseral modes ($m < l$, $m \neq 0$) also contribute. As shown in
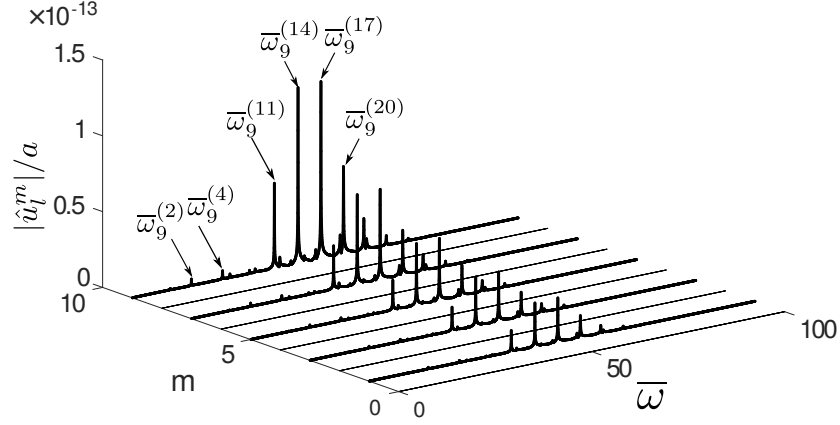
28

Figure 10: FRF $|\hat{u}_l^m(\omega)|/a$ at the surface of a viscoelastic sphere $(r = a)$ for $l = 9$ for the collimating wave $(\theta_\sigma = 0.1514)$.

Fig. 10, the FRF $|\hat{u}_l^m(\omega)|$ for $l = 9$ exhibit several peaks which correspond to resonances of various spheroidal modes (torsional modes are not excited). It can be observed that the leading contributions come from the resonances of the 14th and the 17th spheroidal modes. The resonance of the Rayleigh mode is hence negligible. Therefore in Fig. 9a, the modes with a small polar wavenumber l can be interpreted as the contribution of body waves. It can be inferred that the collimating Rayleigh wave actually corresponds to a superposition of Rayleigh sectoral modes of high wavenumber $m \approx l$, $i.e.$ modes confined near the surface and near the equator of the sphere. This is confirmed by Fig. 11, showing the FRF $|\hat{u}_l^m(\omega)|$ for $l = 52$.

For the diverging and focusing waves, Figs. 8b-c and Figs. 9b-c show that the contribution of tesseral modes is also significant for higher polar wavenumbers l $(l > 30)$, as opposed to the collimating case. In that case,
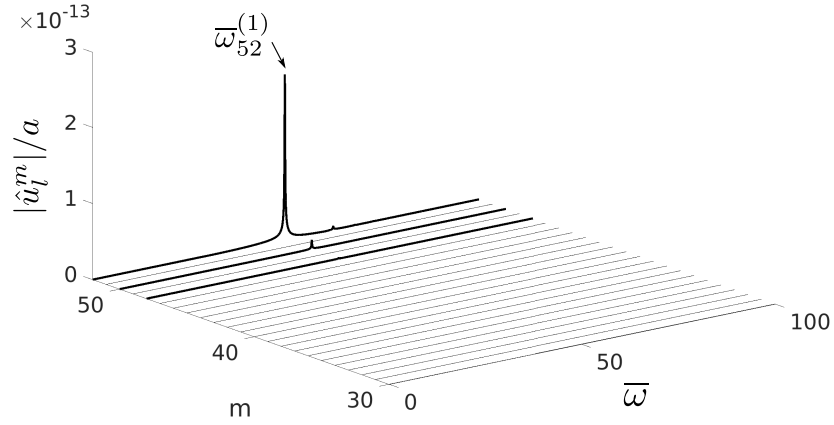
29

Figure 11: FRF $|\hat{u}_l^m(\omega)|/a$ at the surface of a viscoelastic sphere ($r = a$) for $l = 52$ for the collimating wave ($\theta_\sigma = 0.1514$).
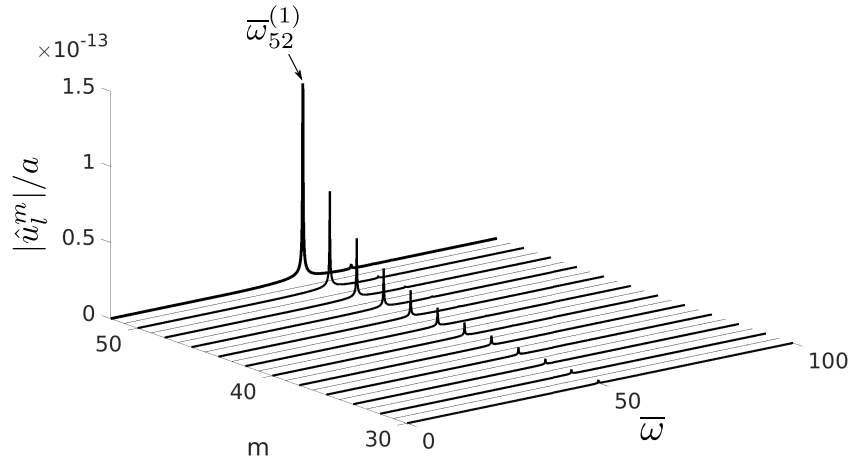

Figure 12: FRF $|\hat{u}_l^m(\omega)|/a$ at the surface of a viscoelastic sphere ($r = a$) for $l = 52$ for the diverging wave ($\theta_\sigma = 0.0667$).

the FRF exhibits a single resonance peak which corresponds to the Rayleigh mode for various values of m (see Fig. 12 for the diverging case at $l = 52$). Therefore, the focusing and diverging waves indeed involve the contribution of Rayleigh tesseral modes ($m \neq l$), in addition to sectoral modes. Note that in the diverging case (Fig. 8c and Fig. 9c), modes with a small polar wavenumber are more excited than in the two other cases. This is an expected result because, as already explained for the collimating source, these low-order modes represent the contribution of body waves, diffracted throughout the sphere.

As a side remark, the similarities between Figs. 8 and 9 tend to show that the type of wave (*i.e.* collimating, focusing or diverging) generated by a source can be qualitatively predicted solely from the a SHT analysis of the force (Fig. 8).

4.3. Effect of a viscoelastic coating

In this last test case, a 1-mm epoxy coating is added at the surface of the sphere (materials properties are given in Table 1). The generation of a collimating wave at the interface between the sphere and the coating is investigated.

The eigenfrequencies of the spheroidal modes of the coated sphere are displayed in Fig. 13 for $n \leq 5$ and the group velocity is plotted in Fig. 14. For the sake of comparison, the curves corresponding to the Rayleigh mode without coating are represented with red crosses. The behaviour of the modes significantly changes with the coating. It can be observed that the modal density increases and that the modes are much more dispersive. In particular, the Rayleigh mode of the sphere is not recovered. However, for some values
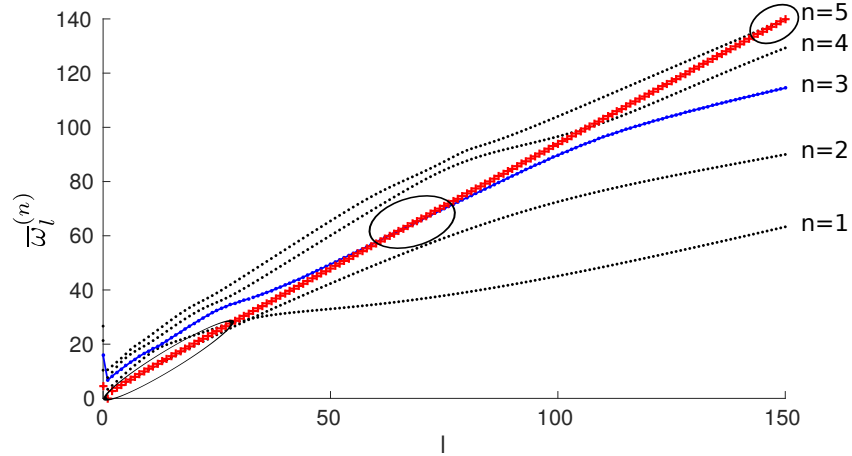
31

Figure 13: Non-dimensional eigenfrequencies $\overline{\omega}_l^{(n)}$ of the spheroidal modes of a viscoelastic steel sphere of radius $a = 25$ mm. Red crosses: Rayleigh mode ($n = 1$) without coating. Bullets: modes with a 1-mm coating of epoxy (in blue, the quasi-Rayleigh mode).
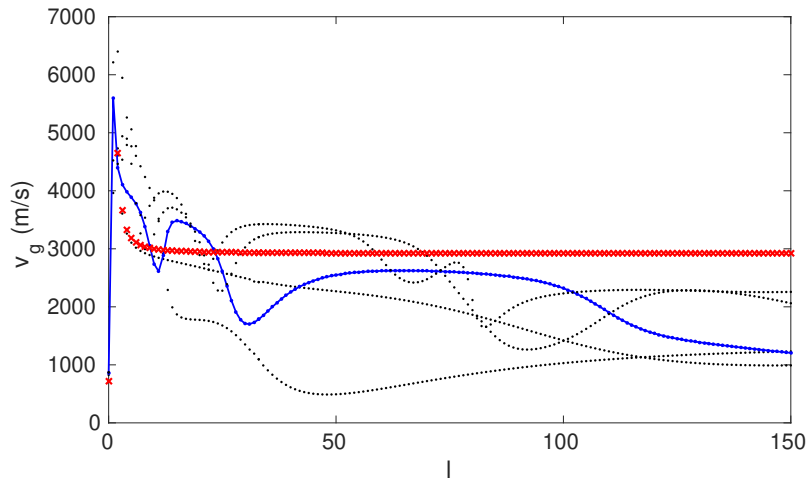

Figure 14: Group velocity of the spheroidal modes of a viscoelastic steel sphere of radius $a = 25$ mm. Red crosses: Rayleigh mode ($n = 1$) without coating. Bullets: modes with a 1-mm coating of epoxy (in blue, the quasi-Rayleigh mode).

32

of l the eigenfrequencies of the coated sphere almost coincide with those of the Rayleigh mode of the surface-free sphere (see the circled zone in Fig. 13). Group velocities can then be locally close to that of the Rayleigh wave. In Fig. 14, the group velocity of the mode identified with blue points is almost non dispersive for $50 < l < 100$. Its value (2620 m s^{-1}) is ten percent lower than the Rayleigh wave velocity of the sphere. The modal attenuations (not shown here for conciseness) are also almost equal in this region. For simplicity, this mode will be called quasi-Rayleigh mode in the following.

Since the collimating wave is a superposition of Rayleigh modes (see Sec. 4.2.2), the source is modified to select the quasi-Rayleigh mode when it is similar to the Rayleigh mode without coating (*i.e.* for $50 < l < 100$). The frequency bandwidth is reduced and centred on a higher frequency (the transient source $g(t)$ is a sinus of centre frequency $f_c = 1.2$ MHz modulated over 10 cycles). The spatial profile $f(\theta, \phi)$ of the source is modified according to Eq. (52). The source is applied in the normal direction and at the interface between the sphere and the coating.

The forced response $u_r(t)$ at the interface and for $\theta = \pi/2$, $\phi = \pi/2$ is shown in Fig. 15. As in the surface-free sphere (in Fig. 5), several major peaks are observed. The time-of-flight between the peaks is equal to 30.31 μs. It yields a velocity of 2591 m s^{-1}, which is quite close to the group velocity of the quasi-Rayleigh mode. Actually, this mode prevails in the FRF (not shown here) which confirms the modal selectivity of the chosen source. Figure 16 represents the normal displacement $u_r(\theta)$ at $\phi = 0$ (blue dashed line) and $\phi = \pi/2$ (red solid line). The amplitude of the wavefront varies, but its width is nearly constant, which means that a collimating wave can be generated at
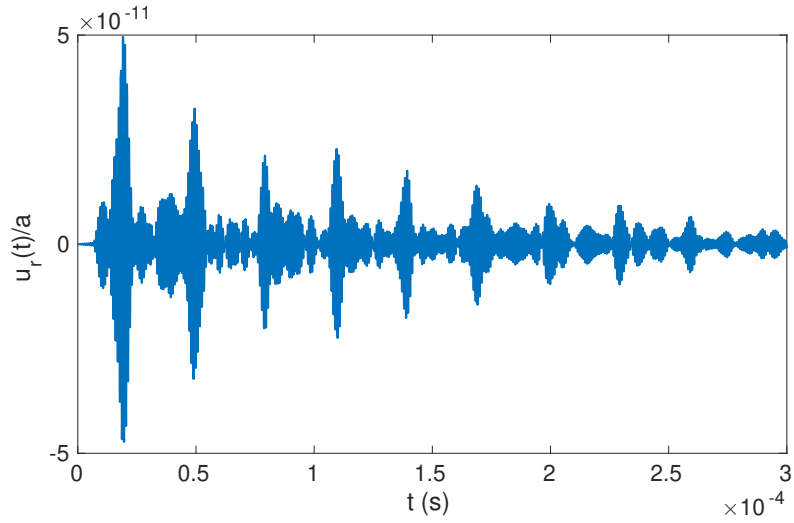
Figure 15: Transient collimating signal $u_r(t)/a$ at the surface $(r = a)$ of a viscoelastic sphere coated with epoxy at point $\theta = \pi/2$, $\phi = \pi/2$. Source parameter: $\theta_\sigma = 0.1514$.
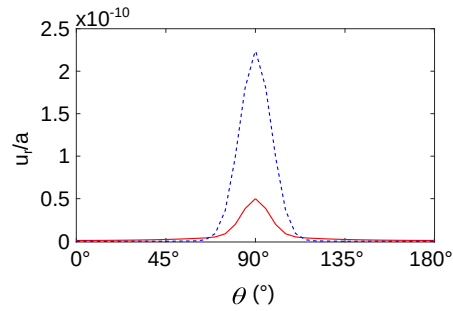

Figure 16: Normal displacement $u_r(\theta)/a$ at the surface $(r = a)$ of a viscoelastic sphere coated with epoxy. Blue dashed curve: at $\phi = 0$ and $t = 4.669$ μs. Red solid curve: at $\phi = \pi/2$ and $t = 19.14$ μs. Source parameter: $\theta_\sigma = 0.1514$.

34

the interface.

5. Conclusion

A semi-analytical one-dimensional finite element formulation has been proposed to compute the free and the forced responses of multi-layered spheres. The solution along the radial coordinate has been approximated with one-dimensional finite elements. Taking advantage of both vector and tensor spherical harmonics orthogonality, the appropriate choice of test function has led to independent governing equations for each couple of angular wavenumbers. A fully analytical description of the angular behaviour of the displacement fields as well as a general formulation suitable for any interpolating technique has been eventually obtained. The formulation yields a linear eigenvalue problem which is simple and fast to solve. The eigensolutions give both the spheroidal and torsional modes. The accuracy of the model has been checked by comparison with literature results for a homogeneous sphere.

The vibration modes have been superposed to reconstruct surface acoustic waves phenomena in the sphere. A collimating Rayleigh wave has then been recovered numerically. The modal analysis of such a wave, based on the resonances of the sphere, has shown that the collimating Rayleigh wave corresponds to a superposition of the fundamental spheroidal modes with a displacement confined at the equator of the sphere: the so-called Rayleigh modes, of sectoral type, with a high polar wavenumber. When the sphere is coated with a thin elastic layer, the numerical results have shown that the Rayleigh mode behaviour is approximately recovered in a limited fre-

quency range. This allows generating a collimating wave at the interface of the sphere and the coating.

Further works are currently in progress to model and study the influence of an infinite embedding medium on the free vibrations and surface wave propagation in spherical structures.

Acknowledgement

36

Appendix A. Properties of spherical harmonics

Appendix A.1. Scalar orthogonality relationships

First, let us recall that the normalized spherical harmonics form an orthonormal basis, such that [25]:

$$\int_0^\pi \int_0^{2\pi} Y_k^{p*} Y_l^m \mathrm{d}\phi \sin\theta \mathrm{d}\theta = \delta_{kl}\delta_{mp}\,. \tag{A.1}$$

Integrating by parts and using the Legendre equation (6), one can show that [15]:

$$\int_0^\pi \int_0^{2\pi} \left[\frac{\partial Y_k^{p*}}{\partial\theta}\frac{\partial Y_l^m}{\partial\theta} + \frac{1}{\sin^2\theta}\frac{\partial Y_k^{p*}}{\partial\phi}\frac{\partial Y_l^m}{\partial\phi}\right] \mathrm{d}\phi \sin\theta \mathrm{d}\theta = \bar{l}\delta_{kl}\delta_{mp}\,. \tag{A.2}$$

Furthermore, it can be readily shown that:

$$\int_0^\pi \int_0^{2\pi} \left[\frac{\mathrm{d}Y_k^{p*}}{\mathrm{d}\theta}Y_l^m + Y_k^{p*}\frac{\mathrm{d}Y_l^m}{\mathrm{d}\theta}\right] \mathrm{d}\phi \sin\theta \mathrm{d}\theta = 0\,. \tag{A.3}$$

These three scalar relationships yields the orthogonality of vector spherical harmonics, expressed by Eq. (12), and are also useful to evaluate some components of the stiffness and mass matrices.

Other relationships are necessary to evaluate the integral of $\delta\epsilon^{\mathrm{T}}\sigma$ in Eq. (1). These relations are [17]:

$$\int_0^\pi \int_0^{2\pi} \left[\left(\frac{\partial^2 Y_k^{p*}}{\partial\theta^2} - \cot\theta\frac{\partial Y_k^{p*}}{\partial\theta} - \frac{1}{\sin^2\theta}\frac{\partial^2 Y_k^{p*}}{\partial\phi^2}\right)\left(\frac{\partial^2 Y_l^m}{\partial\theta^2} - \cot\theta\frac{\partial Y_l^m}{\partial\theta} - \frac{1}{\sin^2\theta}\frac{\partial^2 Y_l^m}{\partial\phi^2}\right)\right.$$
$$\left.+4\frac{\partial}{\partial\theta}\left(\frac{1}{\sin\theta}\frac{\partial Y_k^{p*}}{\partial\phi}\right)\frac{\partial}{\partial\theta}\left(\frac{1}{\sin\theta}\frac{\partial Y_l^m}{\partial\phi}\right)\right] \mathrm{d}\phi \sin\theta \mathrm{d}\theta = (l-1)\bar{l}(l+2)\delta_{kl}\delta_{mp},$$
$$\tag{A.4}$$

37

$$\int_0^\pi \int_0^{2\pi} \left[-\frac{\partial}{\partial \theta} \left(\frac{1}{\sin \theta} \frac{\partial Y_k^{p*}}{\partial \phi} \right) \left(\frac{\partial^2 Y_l^m}{\partial \theta^2} - \cot \theta \frac{\partial Y_l^m}{\partial \theta} - \frac{1}{\sin^2 \theta} \frac{\partial^2 Y_l^m}{\partial \phi^2} \right) \right.$$
$$\left. + \frac{\partial}{\partial \theta} \left(\frac{1}{\sin \theta} \frac{\partial Y_l^m}{\partial \phi} \right) \left(\frac{\partial^2 Y_k^{p*}}{\partial \theta^2} - \cot \theta \frac{\partial Y_k^{p*}}{\partial \theta} - \frac{1}{\sin^2 \theta} \frac{\partial^2 Y_k^{p*}}{\partial \phi^2} \right) \right] d\phi \sin \theta d\theta = 0.$$

(A.5)

The above results, which are given in a scalar form in this paper for the sake of simplicity, must actually be derived from the orthogonality properties of tensor spherical harmonics. This derivation is more mathematically involved than for vector spherical harmonics [16]. These tensorial properties can be found under a compact dyadic form in the work of Martinec [17].

Appendix A.2. Derivative with respect to the polar angle

To evaluate the value of the matrix $\mathbf{S}_l^m$ at any angular coordinates, it is necessary to compute the derivative $\frac{\partial Y_l^m}{\partial \theta}$. Convenient formulas are given by Bosch [40] to avoid singular values at poles. These formulas have been slightly modified to be consistent with the normalization chosen in this paper, based on the guidelines of Ref. [40, Appendix A], denoting $\overline{P}_l^m(\cos \theta) = N_l^m P_l^m(\cos \theta)$.

The polar derivative of a spherical harmonic can be obtained using the following recurrence formula (for $m \geq 0$):

$$2\frac{\partial Y_l^m(\theta, \phi)}{\partial \theta} = \left(\sqrt{(l-m)(l+m+1)}\overline{P}_l^{m+1}(\cos \theta) - \sqrt{(l+m)(l-m+1)}\overline{P}_l^{m-1}(\cos \theta) \right) \frac{e^{jm\phi}}{\sqrt{2\pi}}.$$

(A.6)

For $m < 0$, the derivative can be readily obtained using the equality $Y_l^{-m} = (-1)^m Y_l^m$. The cases of $m = 0$ or $m = l$ are specific and the derivatives are

38

given by:

$$\frac{\partial Y_0^0(\theta, \phi)}{\partial \theta} = 0 \,, \tag{A.7}$$

$$\frac{\partial Y_l^0(\theta, \phi)}{\partial \theta} = \sqrt{\frac{\bar{l}}{4\pi}} \overline{P}_l^1(\cos \theta) \,, \tag{A.8}$$

$$\frac{\partial Y_l^l(\theta, \phi)}{\partial \theta} = -\sqrt{\frac{l}{4\pi}} \overline{P}_l^{l-1}(\cos \theta) \mathrm{e}^{\mathrm{j}l\phi} \,. \tag{A.9}$$

At poles ($\theta = 0$ or $\theta = \pi$), for $m = 0$ the spherical harmonics do not depend on ϕ. From Eq. (5) and using the properties $P_l^0(1) = 1$ and $P_l^0(-1) = (-1)^l$, one gets [25]:

$$Y_l^0(0, \phi) = \sqrt{\frac{2l+1}{4\pi}} \,, \tag{A.10}$$

$$Y_l^0(\pi, \phi) = (-1)^l \sqrt{\frac{2l+1}{4\pi}} \,. \tag{A.11}$$

For $m > 0$, the azimuthal coordinate is undetermined and the spherical harmonics must hence vanish at poles [25].

Similarly, the derivative must vanish at poles for $m \neq 0$. For $m = 0$, using the property $\overline{P}_l^1(\pm 1) = 0$ into Eq. (A.8) enables to show that:

$$\frac{\partial Y_l^0(0, \phi)}{\partial \theta} = \frac{\partial Y_l^0(\pi, \phi)}{\partial \theta} = 0 \,. \tag{A.12}$$

Appendix B. Example: calculation of the component K_{22} of the stiffness matrix

In the following, let us detail for the sake of clarity the computation of the second diagonal component of the stiffness matrix $\mathbf{K}$, denoted K_{22}. The latter is derived from the integral of $\delta\epsilon^{\mathrm{T}}\sigma$ in Eq. (1), where the integrand can

39

be explicitly written:

$$\delta\epsilon^{\mathrm{T}}\sigma = \sum_{l\geq0}\sum_{|m|\leq l}\left[\frac{\partial\delta\hat{\mathbf{u}}^{\mathrm{T}}}{\partial r}\mathbf{S}_k^{p*}\mathbf{L}_r^{\mathrm{T}}\mathbf{C}\mathbf{L}_r\mathbf{S}_l^m\frac{\partial\hat{\mathbf{u}}_l^m}{\partial r}\right.$$

$$+\left(\frac{1}{r}\frac{\partial\delta\hat{\mathbf{u}}^{\mathrm{T}}}{\partial r}\mathbf{S}_k^{p*}\mathbf{L}_r^{\mathrm{T}} + \frac{\delta\hat{\mathbf{u}}^{\mathrm{T}}}{r^2}\frac{\partial\mathbf{S}_k^{p*}}{\partial\theta}\mathbf{L}_\theta^{\mathrm{T}} + \frac{\delta\hat{\mathbf{u}}^{\mathrm{T}}}{r^2\sin\theta}\frac{\partial\mathbf{S}_k^{p*}}{\partial\phi}\mathbf{L}_\phi^{\mathrm{T}} + \frac{\delta\hat{\mathbf{u}}^{\mathrm{T}}}{r^2}\mathbf{S}_k^{p*}\mathbf{L}_1^{\mathrm{T}} + \cot\theta\frac{\delta\hat{\mathbf{u}}^{\mathrm{T}}}{r^2}\mathbf{S}_k^{p*}\mathbf{L}_2^{\mathrm{T}}\right)\mathbf{C}\mathbf{A}_l^m\hat{\mathbf{u}}_l^m$$

$$\left. + \delta\hat{\mathbf{u}}^{\mathrm{T}}\mathbf{A}_k^{p*\mathrm{T}}\mathbf{C}\mathbf{S}_l^m\mathbf{L}_r\frac{1}{r}\frac{\partial\hat{\mathbf{u}}_l^m}{\partial r}\right], \quad \text{(B.1)}$$

where $\mathbf{A}_l^m = \left(\mathbf{L}_\theta\frac{\partial}{\partial\theta}\mathbf{S}_l^m + \frac{1}{\sin\theta}\mathbf{L}_\phi\frac{\partial}{\partial\phi}\mathbf{S}_l^m + \mathbf{L}_1\mathbf{S}_l^m + \cot\theta\mathbf{L}_2\mathbf{S}_l^m\right)$.

Hence, there is 25 matrices to compute using Eqs. (2), (4), (9). In the specific case of the component K_{22}, it yields on one finite element:

$$K_{22} = \sum_{l\geq0}\sum_{|m|\leq l}\int_0^\pi\int_0^{2\pi}\left[\int\delta\hat{\mathbf{u}}^{e\mathrm{T}}\left(\left(\frac{\partial^2 Y_k^{p*}}{\partial\theta^2} + \cot\theta\frac{\partial Y_k^{p*}}{\partial\theta} + \frac{1}{\sin^2\theta}\frac{\partial^2 Y_k^{p*}}{\partial\phi^2}\right)\right.\right.$$

$$\times\left(\frac{\partial^2 Y_l^m}{\partial\theta^2} + \cot\theta\frac{\partial Y_l^m}{\partial\theta} + \frac{1}{\sin^2\theta}\frac{\partial^2 Y_l^m}{\theta\partial\phi^2}\right)C_{23}$$

$$+\left\{2\left(\cot\theta\frac{\partial Y_k^{p*}}{\partial\theta} + \frac{1}{\sin^2\theta}\frac{\partial^2 Y_k^{p*}}{\partial\phi^2}\right)\left(\cot\theta\frac{\partial Y_l^m}{\partial\theta} + \frac{1}{\sin^2\theta}\frac{\partial^2 Y_l^m}{\partial\phi^2}\right) + 2\frac{\partial^2 Y_k^{p*}}{\partial\theta^2}\frac{\partial^2 Y_l^m}{\partial\theta^2}\right.$$

$$\left.+\left(\frac{\partial}{\partial\theta}\left(\frac{1}{\sin\theta}\frac{\partial Y_k^{p*}}{\partial\phi}\right) - \frac{\cot\theta}{\sin\theta}\frac{\partial Y_k^{p*}}{\partial\phi} + \frac{1}{\sin\theta}\frac{\partial^2 Y_k^{p*}}{\partial\phi\partial\theta}\right)\left(\frac{\partial}{\partial\theta}\left(\frac{1}{\sin\theta}\frac{\partial Y_l^m}{\partial\phi}\right) - \frac{\cot\theta}{\sin\theta}\frac{\partial Y_l^m}{\partial\phi} + \frac{1}{\sin\theta}\frac{\partial^2 Y_l^m}{\partial\theta\partial\phi}\right)\right\}$$

$$\left.+\int\left(\delta\hat{\mathbf{u}}^{e\mathrm{T}} - r\frac{\partial\delta\hat{\mathbf{u}}^{e\mathrm{T}}}{\partial r}\right)\left(\frac{1}{\sin^2\theta}\frac{\partial Y_k^{p*}}{\partial\phi}\frac{\partial Y_l^m}{\partial\phi} + \frac{\partial Y_k^{p*}}{\partial\theta}\frac{\partial Y_l^m}{\partial\theta}\right)\left(\hat{\mathbf{u}}^e - r\frac{\partial\hat{\mathbf{u}}_l^{me}}{\partial r}\right)C_{55}\mathrm{d}r\right]\mathrm{d}\phi\sin\theta\mathrm{d}\theta\,.$$

$$\text{(B.2)}$$

It can be immediatly noticed that the terms factored by C_{55} involves the orthogonality relationship (A.2). Noticing that $-\frac{\cot\theta}{\sin\theta}\frac{\partial Y_l^m}{\partial\phi} + \frac{1}{\sin\theta}\frac{\partial^2 Y_l^m}{\partial\theta\partial\phi} = \frac{\partial}{\partial\theta}\left(\frac{1}{\sin\theta}\frac{\partial Y_l^m}{\partial\phi}\right)$, and using the Legendre equation (6), the term factored by C_{44} can be rewritten as:

$$\overline{k}\,\overline{l}Y_k^{p*}Y_l^m + \left(\frac{\partial^2 Y_k^{p*}}{\partial\theta^2} - \cot\theta\frac{\partial Y_k^{p*}}{\partial\theta} - \frac{1}{\sin^2\theta}\frac{\partial^2 Y_k^{p*}}{\partial\phi^2}\right)\left(\frac{\partial^2 Y_l^m}{\partial\theta^2} - \cot\theta\frac{\partial Y_l^m}{\partial\theta} - \frac{1}{\sin^2\theta}\frac{\partial^2 Y_l^m}{\partial\phi^2}\right)$$

$$+ 4\frac{\partial}{\partial\theta}\left(\frac{1}{\sin\theta}\frac{\partial Y_k^{p*}}{\partial\phi}\right)\frac{\partial}{\partial\theta}\left(\frac{1}{\sin\theta}\frac{\partial Y_l^m}{\partial\phi}\right), \quad \text{(B.3)}$$

where $\bar{k} = k(k+1)$. This term involves orthogonality relationships (A.1) and (A.4). Finally, the two terms factored by C_{23} can be replaced using the Legendre equation (6) and further simplified using the orthogonality relationship (A.1). This yields:

$$K_{22} = \int \delta\hat{\mathbf{u}}^{e\mathrm{T}} \left(\bar{l}^2 C_{23} + 2\bar{l}(\bar{l}-1)C_{44} \right) \hat{\mathbf{u}}_l^{me}\mathrm{d}r + \int \left(\delta\hat{\mathbf{u}}^{e\mathrm{T}} - r\frac{\partial \delta\hat{\mathbf{u}}^{e\mathrm{T}}}{\partial r} \right) \bar{l}C_{55} \left(\hat{\mathbf{u}}^e - r\frac{\partial \hat{\mathbf{u}}^e}{\partial r} \right) \mathrm{d}r.$$
(B.4)

Using the finite element interpolation (14), one finally recasts the second diagonal component of the elementary matrices of Eqs. (17)–(19).

[1] H. Lamb. On the vibrations of an elastic sphere. *Proceedings of the London Mathematical Society*, 1(1):189–212, 1881.

[2] K. Sezawa. Dispersion of elastic waves propagated on the surface of stratified bodies and on curved surfaces. *Bulletin of the Earthquake Research Institute Tokyo*, 3:1–18, 1927.

[3] Y. Sato and T. Usami. Basic study on the oscillation of a homogeneous elastic sphere I. frequency of the free oscillation. *Geophys. Mag*, 31: 15–24, 1962.

[4] K. Aki and P. G. Richards. *Quantitative Seismology, Theory and Methods*, volume 1. 1980.

[5] A. H. Shah, C. V. Ramkrishnan, and S. K. Datta. Three-dimensional and shell-theory analysis of elastic waves in a hollow sphere: Part 1—analytical foundation. *Journal of Applied Mechanics*, 36(3):431–439, 1969.

[6] P. R. Heyliger and A. Jilani. The free vibrations of inhomogeneous elastic cylinders and spheres. *International Journal of Solids and Structures*, 29(22):2689–2708, 1992.

[7] W. Q. Chen and H. J. Ding. Free vibration of multi-layered spherically isotropic hollow spheres. *International Journal of Mechanical Sciences*, 43(3):667–680, 2001.

[8] T. Ye, G. Jin, and Z. Su. Three-dimensional vibration analysis of laminated functionally graded spherical shells with general boundary conditions. *Composite Structures*, 116:571–588, 2014.

[9] K. L. Williams and P. L. Marston. Axially focused (glory) scattering due to surface waves generated on spheres: Model and experimental confirmation using tungsten carbide spheres. *The Journal of the Acoustical Society of America*, 78(2):722–728, 1985.

[10] L. Saviot, D. B. Murray, and M. D. C. M. De Lucas. Vibrations of free and embedded anisotropic elastic spheres: Application to low-frequency Raman scattering of silicon nanoparticles in silica. *Physical Review B*, 69(11):113402, 2004.

[11] S. Petit, M. Duquennoy, M. Ouaftouh, F. Deneuville, M. Ourak, and S. Desvaux. Non-destructive testing of ceramic balls using high frequency ultrasonic resonance spectroscopy. *Ultrasonics*, 43(10):802–810, 2005.

[12] G. R. Buchanan and G .R. Ramirez. A note on the vibration of transversely isotropic solid spheres. *Journal of Sound and Vibration*, 253(3): 724–732, 2002.

[13] J. Park. *Wave motion in finite and infinite media using the thin-layer method.* PhD thesis, Massachusetts Institute of Technology, 2002.

[14] Hauke Gravenkamp, Albert A Saputra, and Sascha Duczek. High-order shape functions in the scaled boundary finite element method revisited. *Archives of Computational Methods in Engineering*, pages 1–22, 2019.

[15] E. Kausel. *Fundamental solutions in elastodynamics: a compendium.* Cambridge University Press, 2006.

[16] R. W. James. New tensor spherical harmonics, for application to the partial differential equations of mathematical physics. *Philosophical Transactions of the Royal Society of London. Series A, Mathematical and Physical Sciences*, 281(1302):195–221, 1976.

[17] Z. Martinec. Spectral–finite element approach to three-dimensional viscoelastic relaxation in a spherical earth. *Geophysical Journal International*, 142(1):117–141, 2000.

[18] Juliette Chabassier and Marc Duruflé. High order finite element method for solving convected helmholtz equation in radial and axisymmetric domains. application to helioseismology. Technical report, INRIA, 2016.

[19] A. C. Eringen and E. S. Şuhubi. *Elastodynamics*, volume II. Academic Press, 1975.

[20] Y. Tsukahara, H. Nakaso, N.and Cho, and K. Yamanaka. Observation of diffraction-free propagation of surface acoustic waves around a homogeneous isotropic solid sphere. *Applied Physics Letters*, 77(18):2926–2928, 2000.

[21] S. Ishikawa, N. Nakaso, N. Takeda, T. Mihara, Y. Tsukahara, and K. Yamanaka. Surface acoustic waves on a sphere with divergent, focusing, and collimating beam shapes excited by an interdigital transducer. *Applied physics letters*, 83(22):4649–4651, 2003.

[22] D. Clorennec and D. Royer. Investigation of surface acoustic wave propagation on a sphere using laser ultrasonics. *Applied physics letters*, 85 (12):2435–2437, 2004.

[23] K. Yamanaka, N. Nakaso, D. Sim, and T. Fukiura. Principle and application of ball surface acoustic wave (SAW) sensor. *Acoustical science and technology*, 30(1):2–6, 2009.

[24] K.J. Bathe. *Finite Element Procedures*. Prentice-Hall, Englewood Cliffs, 1995. ISBN 0-13-301458-4.

[25] G. B. Arfken and H. J. Weber. *Mathematical methods for physicists*. AAPT, 1999.

[26] K. L. J. Fong. *A study of curvature effects on guided elastic waves*. PhD thesis, University of London, 2005.

[27] A. Silbiger. Nonaxisymmetric modes of vibration of thin spherical shells. *The Journal of the Acoustical Society of America*, 34(6):862–862, 1962.

[28] T. A. Duffey, J. E. Pepin, A. N. Robertson, M. L. Steinzig, and K. Coleman. Vibrations of complete spherical shells with imperfections. *Journal of Vibration and Acoustics*, 129(3):363–370, 2007.

[29] J. N. Brune, J. E. Nafe, and L. E. Alsop. The polar phase shift of surface waves on a sphere. *Bulletin of the Seismological Society of America*, 51 (2):247–257, 1961.

[30] S. Finnveden. Evaluation of modal density and group velocity by a finite element method. *Journal of Sound and Vibration*, 273(1-2):51–75, 2004.

[31] P. J. Kostelec, D. K . Maslen, D. M. Healy Jr, and D. N. Rockmore. Computational harmonic analysis for tensor fields on the two-sphere. *Journal of Computational Physics*, 162(2):514–535, 2000.

45

[32] D. M. Healy, D. N. Rockmore, P. J. Kostelec, and S. Moore. FFTs for the 2-Sphere-Improvements and Variations. *Journal of Fourier Analysis and Applications*, 9(4):341–385, 2003. ISSN 1531-5851. doi: 10.1007/s00041-003-0018-9.

[33] M. A. Wieczorek and M. Meschede. Shtools: Tools for working with spherical harmonics. *Geochemistry, Geophysics, Geosystems*, 19(8): 2574–2592, 2018.

[34] N. Schaeffer. Efficient spherical harmonic transforms aimed at pseudospectral numerical simulations. *Geochemistry, Geophysics, Geosystems*, 14(3):751–758, 2013.

[35] M. Frigo and S. G. Johnson. FFTW: An adaptive software architecture for the FFT. In *Proceedings of the 1998 IEEE International Conference on Acoustics, Speech and Signal Processing, ICASSP'98 (Cat. No. 98CH36181)*, volume 3, pages 1381–1384. IEEE, 1998.

[36] J. C. Knight, N. Dubreuil, V. Sandoghdar, J. Hare, V. Lefèvre-Seguin, J. M. Raimond, and S. Haroche. Mapping whispering-gallery modes in microspheres with a near-field probe. *Optics Letters*, 20(14):1515–1517, 1995. doi: 10.1364/OL.20.001515.

[37] A. N. Oraevsky. Whispering-gallery waves. *Quantum electronics*, 32(5): 377, 2002.

[38] M. R. Foreman, J. D. Swaim, and F. Vollmer. Whispering gallery mode sensors. *Advances in optics and photonics*, 7(2):168–240, 2015.

681 [39] N. Hale T. A. Driscoll and L. N. Trefethen. *Chebfun Guide.* Pafnuty
682   Publication, Oxford, 2014.

683 [40] W. Bosch. On the computation of derivatives of Legendre functions.
684   *Physics and Chemistry of the Earth, Part A: Solid Earth and Geodesy,*
685   25(9-11):655–659, 2000.